García-Fayos, J.; Ruhl, R.; Navarrete Algaba, L.; Bouwmeester, H.; Serra Alfaro, JM. (2018). Enhancing oxygen permeation through Fe2NiO4-Ce0.8Tb0.2O2-delta composite membranes using porous layers activated with Pr6O11 nanoparticles. Journal of Materials Chemistry A. 6(3):1201-1209. https://doi.org/10.1039/c7ta06485c

Enhancing oxygen permeation through Fe_2NiO_4-$Ce_{0.8}Tb_{0.2}O_{2-\delta}$ composite membranes using porous layers activated with Pr_6O_{11} nanoparticles

Julio García-Fayos[1], Rian Ruhl[2], Laura Navarrete[1], Henny J. M. Bouwmeester[2,*], Jose M. Serra[1,*]

[1]*Instituto de Tecnología Química (Universitat Politècnica de València – Consejo Superior de Investigaciones Científicas), av. Los Naranjos s/n, E-46022 Valencia, Spain Tel: +34 96 3879448 e-mail: jmserra@itq.upv.es*

[2]*Electrochemistry Research Group, Membrane Science and Technology, Faculty of Science and Technology, MESA+ Institute for Nanotechnology, University of Twente, The Netherlands*

Abstract

Fe_2NiO_4–$Ce_{0.8}Tb_{0.2}O_{2-\delta}$ (NFO-CTO) composite membranes are of interest to separate oxygen from air. In this study, we investigate the influence of the catalytic activation of NFO-CTO membranes on the oxygen permeation rate. Specifically, the effect of activating porous NFO-CTO layers – sandwiched on both sides of the dense NFO-CTO membrane – with Pr_6O_{11} nanoparticles is studied. Measurements in the temperature range 850 – 700 ºC revealed a 2-4 fold increase in the oxygen flux after coating a 30-μm-thick porous NFO-CTO layer on both membrane sides, and a 6-12 fold increase relative to the bare membrane after activating the porous layers with Pr_6O_{11} nanoparticles into both coated layers. No degradation of the oxygen fluxes was found in CO_2-containing atmospheres. Pulse isotopic exchange measurements confirmed an increase in the oxygen surface exchange rate of more than one order of magnitude after dispersion of Pr_6O_{11} nanoparticles on the surface of NFO-CTO composite powders. Electrochemical impedance spectroscopy measurements on symmetrical cells, using Gd-doped ceria (CGO) as the electrolyte and Pr_6O_{11}-activated NFO-CTO electrodes, showed a 10-fold decrease in the polarization resistance compared to non-infiltrated electrodes in air. Modification of porous layers by activation with Pr_6O_{11} nanoparticles is considered a viable route to enhance the oxygen fluxes across composite membranes.

Keywords:

Dual-phase membranes; oxygen transport membranes; infiltration; Pr_6O_{11}; nanoparticles; catalyst

1. Introduction

The production of oxygen is a key step in several industrial processes. Approximately 150 million tons of oxygen are produced each year [1], setting oxygen as the third largest chemical commodity worldwide [2]. Main applications are industrial manufacture (in particularly in the steel industry), power generation and medical uses. In addition, process efficiencies can in some industrial applications be enhanced by using pure oxygen instead of air. This is especially the case for power generation applications, in which the use of pure oxygen improves overall process efficiency and avoids emission of greenhouse gases. Combustion in oxygen-rich atmospheres leads to an increase of the flame temperature, either reducing the fuel consumption or enabling the use of alternative fuels with lower heat capacity (and lower cost). Moreover, mass and volume of flue gases are considerably reduced (up to 75%), and therefore smaller installations and equipment are needed, reducing capital and O&M costs. As a result of using oxygen-rich streams, flue gases mainly consist of CO_2 and H_2O. CO_2 can be easily separated from H_2O by condensing the water, yielding a pure stream of CO_2. Once purified, CO_2 can be utilized in several industrial processes, such as supercritical applications, carbonation of beverages, polymer foam blowing, urea production and medical gases [3]. Cryogenic distillation of air is presently the standard technology for the production of pure oxygen. Nevertheless, high energy costs and the need of huge installations make the application of this technology economically unfeasible for most of the target applications [4]. Therefore, oxygen transport membrane (OTM) technology is presented as an appealing alternative for the supply of oxygen in small and medium-scale installations [5-7].

Since the pioneering works on OTMs in the 70s [8-10], and after a large number of studies during the last decades, several materials with high oxygen permeation rates have been developed [11, 12]. Despite the high oxygen fluxes reached with perovskite-type oxides like $Ba_{0.5}Sr_{0.5}Co_{0.2}Fe_{0.8}O_{3-\delta}$ (BSCF), issues such as a lack of mechanical and chemical stability [13] and a complete loss in performance when exposed to CO_2-containing environments [14-16], limit their industrial applicability. To overcome these, several groups are developing CO_2-stable dual-phase materials [17-19]. Amongst all studied materials, one of the most promising is the dual phase composite 60-40 vol% Fe_2NiO_4 –$Ce_{0.8}Tb_{0.2}O_{2-\delta}$ (NFO-CTO) [20-22]. This spinel-fluorite dual-phase material has been studied under oxyfuel-like environments with excellent results in terms of stability [20-22] and performance, i.e. thin NFO-CTO membranes deposited on LSCF freeze-casted supports reached oxygen fluxes above 1-2 ml min^{-1} cm^{-2} under CO_2-containing environments at 850 ºC [21]. However, the fluxes are still below 5-10 ml min^{-1} cm^{-2}, which are required to ensure techno-economic feasibility of OTMs [23]. Strategies to optimize the performance of OTMs include reduction of membrane thickness and surface modification, especially via catalytic activation. The latter represents an effective method for improving the oxygen fluxes when the oxygen fluxes are limited by the surface exchange kinetics, i.e. for relatively thin membranes and/or at intermediate temperatures (below 800 ºC). The addition of a porous layer can enhance the membrane performance by increasing the specific surface area and thereby increasing the number of active sites for oxygen exchange [24, 25]. For composite materials, these are the triple phase boundaries (TPB) where the gas phase meets the ionic and electronic conducting phases and where oxygen incorporation and release reactions occur. As sketched in Figure 1, the fine-grained porous layer provides a much larger number of TPB sites than the bare membrane surface. The porous layers are of a similar composition as the dense layer to warranty thermo-mechanical compatibility.

In recent years, infiltration of active components into porous scaffolds has been gaining increased attention to enhance the performance of SOFC electrodes [26], as previously practiced to improve the performance of $La_{0.8}Sr_{0.2}MnO_{3-\delta}$-$Ce_{0.8}Gd_{0.2}O_{2-\delta}$ cathodes [27]. Following previous studies of modification of SOFC cathodes by infiltration with praseodymium oxide (Pr_6O_{11}) nanoparticles [27-29], the present work focuses on enhancing the oxygen permeation rate of Fe_2NiO_4–$Ce_{0.8}Tb_{0.2}O_{2-\delta}$ (NFO-CTO) dual-phase composite membranes. This is achieved by activating the porous NFO-CTO layers with Pr_6O_{11}.–coated on both membrane sides. Electrochemical impedance spectroscopy (EIS) and pulse isotopic exchange (PIE) are used to investigate the influence of Pr_6O_{11} activation on surface exchange kinetics.

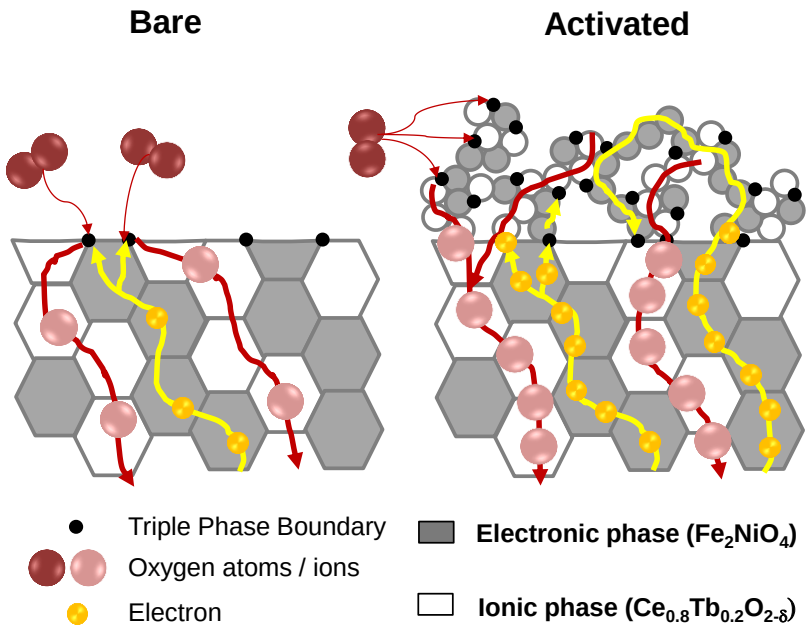

Figure 1: Schematics showing the ionic and electronic percolative paths and the distribution of TPB sites for an NFO-CTO composite membrane with and without a porous activation layer (of similar composition). Transport of oxygen ions and electrons in the activation layer is enabled via percolative pathways for both charge carriers.

2. Experimental

2.1. Samples preparation

NFO and 60% NFO – 40% CTO composite powders were prepared via a one-pot Pechini process. To this end, corresponding metal nitrates were dissolved in distilled water ($Ce(NO_3)_3 \cdot 6H_2O$, and $Fe(NO_3)_3 \cdot 9H_2O$ were provided by Sigma Aldrich, $Tb(NO_3)_3 \cdot 6H_2O$ and $Ni(NO_3)_3 \cdot 6H_2O$ by ABCR GmbH). Subsequently, citric acid (Sigma Aldrich) and ethylene glycol were added as chelating and gelating agents in a molar ratio of metal:citric acid:ethylene glycol 1:2:4. After drying (up to 270 °C), the obtained gel was fired at 600 °C to obtain finely dispersed powders with the correct structural phases, as confirmed by X-ray diffraction (XRD). Dense NFO and NFO-CTO ceramics were obtained by uniaxial pressing of the corresponding powders at 125 MPa, followed by sintering of the obtained disks in air at 1400 °C for 10 h (2 °C min^{-1} heating rate, 5 °C min^{-1} cooling

rate). For oxygen permeation measurements, membranes with a diameter of 15 mm and thicknesses of 0.6-0.7 mm were obtained from the sintered NFO-CTO disks after grinding and polishing with sandpaper.

Powders of CTO and $Ce_{0.8}Gd_{0.2}O_{1.9}$ (CGO) were synthesized by the co-precipitation method [30]. CGO was co-doped with cobalt to improve the sinterability of the powder. This was done by impregnating $Co(NO_3)_2 \cdot 6H_2O$ dissolved in deionized water to reach a final 2 mol % content. The obtained powders were calcined in air at 800 ºC for 5h. Dense ceramics were obtained after uniaxial pressing of the powders, followed by sintering the obtained disks in air at 1480 ºC for 4 h (2 ºC min^{-1} heating rate, 5 ºC min^{-1} cooling rate). The densities of all the samples were checked by Archimedes and SEM (Figure S1), resulting in values above 98%.

For EIS and oxygen permeation measurements, 30-μm-thick porous layers of NFO-CTO were screen-printed on both sides of either CGO electrolyte disks or NFO-CTO membranes. Ink for screen-printing was made by mixing a 1:2 weight ratio of NFO-CTO powder previously ball-milled for 8 h and an ethyl cellulose (6 wt%) solution in terpineol in a three roll mill. After deposition, the obtained composite ceramic structures were sintered in air at 1100 ºC for 2 h. Catalytic activation of the porous NFO-CTO scaffold layers was accomplished by infiltration, ensuring proper dispersion of catalyst particles [31]. To this end, a 2 M solution of $Pr(NO_3)_3 \cdot 6H_2O$ (Sigma Aldrich) in ethanol-water (in a volume ratio 1:1) was dripped onto the porous composite scaffold layers, being infiltrated by capillary forces. After infiltration, the samples were dried at 80 ºC for 1 h, and calcined in air at 850 ºC for 2 h.

NFO, CTO and NFO-CTO composite powders for PIE measurements were obtained by crushing dense sintered ceramics, and subsequent sieving of the obtained powder through a 100 μm mesh. Composite powders for PIE measurements were activated with Pr_6O_{11} nanoparticles by incipient wetness impregnation using a 2 M solution of $Pr(NO_3)_3 \cdot 6H_2O$ (Sigma Aldrich) in ethanol-water (in a volume ratio 1:1) and subsequent calcination for 2 h at 850 ºC in air.

2.2. Samples characterization

2.2.1. Microstructural study

Identification of the crystalline phases of the samples was done by means of X-ray diffraction (XRD). The measurements were carried out using a PANalytical CubiX fast diffractometer, using CuKα1 radiation (λ = 1.5406 Å) and a X'Celerator detector in Bragg−Brentano geometry. XRD patterns recorded in the 2θ range from 10° to 90° were analyzed using X'Pert Highscore Plus software. Scanning Electron Microscopy (SEM) and Energy-dispersive X-ray spectroscopy (EDX) analyses were performed using a ZEISS Ultra55 field emission scanning electron microscope. In these experiments, cross sections of the membranes before and after the permeation tests were analyzed. A backscattered electron detector (BSD) was used for investigating the distribution of the phases in the dual-phase composite.

2.2.2. PIE measurements

PIE measurements were conducted using a home-made set-up [32]. The powder sample was loaded in the centre of a quartz tubular micro-reactor with an inner diameter of 2 mm. Quartz wool plugs were used to secure the packed powder bed. The length and mass of the packed bed were typically 10 mm and 0.08 g, respectively. $^{16}O_2$ mixed with Ar was used as carrier gas, and fed through the reactor with a total flow rate of 30 ml min^{-1} (NTP). Gases were dried using Agilent gas clean moisture filters before entering the reactor. Oxygen isotope gas was purchased from Cambridge Isotope Laboratories, Inc. (> 97 atom% $^{18}O_2$). A six-port valve with a 500 µl sample loop was used for injection of the $^{18}O_2/N_2$ pulse into the $^{16}O_2$/Ar carrier gas, the pulse having the same pO_2 as the carrier gas. The diluent nitrogen in the pulse was used for internal calibration of the mass spectrometer (Omni Star TM GSD 301 Pfeiffer-Vacuum). The mean residence time of the reactor varied between 10 and 30 ms, depending on temperature. Prior to measurements, the sample was pre-treated at 850 °C for 2 h (heating rate 5 °C min^{-1})to remove possibly adsorbed water and CO_2, and subsequently cooled to 50 °C at rate of 5 °C min^{-1}. Measurements were performed at a pO_2 of 0.21 atm. Averaged values of the $^{18}O_2$ and $^{16}O^{18}O$ effluent fractions in three pulse experiments, at a given temperature, were used for calculation of the exchange rate. The reactor was equilibrated prior to each measurement before data acquisition. The overall surface exchange rate, $\Re_0$ [mol (O) m^{-2} s^{-1}], was calculated from [33, 34]

$$\Re_0 = \frac{2F_m}{S}\ln\left(\frac{f_i^{18}}{f_e^{18}}\right) \qquad (1)$$

where f_i^{18} and f_e^{18} are the ^{18}O isotope fractions in the pulse at the inlet and exit of the reactor, respectively, F_m is the molar flow rate of oxygen through the packed bed, S the total surface area of the sample. The fraction f^{18} is calculated from $f^{18} = 0.5f^{34} + f^{36}$.

2.2.3. Electrochemical impedance spectroscopy

NFO-CTO/CGO/NFO-CTO symmetrical cells for two-electrode impedance measurements were prepared by coating 30 µm-thick NFO-CTO layers onto both sides of a 0.8 mm-thick CGO electrolyte disks. Measurements were performed at zero bias and an excitation voltage of 20 mV in the frequency range 0.01 – 3·10^5 Hz, using a Solartron 1470E multichannel potentiostat and a 1455A frequency response analyzer. Measurements were performed at 850 ºC, under different atmospheres (N_2, CO_2) and at different pO_2 (0.05-0.21 bar). In all cases, the total flow remained constant (100 ml min^{-1}). The impedance spectra were analysed using ZView®2 software. The impedance spectra were fitted using the equivalent circuit $LR_e(R_1Q_1)(R_2Q_2)(R_3Q_3)$, where L is an inductance, R_e the apparent electrolyte resistance, R_i (i = 1,2,3) a resistance, and Q_i (i = 1,2,3) a constant phase element.

2.2.4. Oxygen permeation measurements

Oxygen permeation studies were carried out in a lab-scale quartz reactor. Synthetic air (100 ml min^{-1}) was used as feed gas, while pure argon or a gas mixture containing 30 vol% CO_2, balance argon, were used as sweep gases (150 ml min^{-1}). Both gas streams were at atmospheric pressure. The temperature was measured by a thermocouple attached to the membrane. A PID controller maintained the temperature within 2 ºC of the set point. Sealing was achieved using Au and Ag O-rings applying different sealing temperatures, i.e. 1000 ºC and 850 ºC, respectively. The bare membrane was sealed with Au O-rings whereas Ag O-rings were used for sealing activated membranes. This was done in order to avoid coarsening phenomena of catalyst particles at higher temperatures. The permeate gas stream was analyzed by online gas chromatography, using a micro-GC Varian CP-4900 equipped with Molsieve5A, Pora-Plot-Q glass capillary, and CP-Sil modules. The leakage of oxygen was subtracted in the calculation of the oxygen flux. The contribution of leakage to the apparent oxygen flux was below 3% in all cases. The data reported here were all obtained after steady state was achieved. Each measurement was repeated three times to minimize the experimental error, which was typically below 0.5%.

3. Results and discussion

3.1. Microstructural study

SEM analyses were conducted on membranes with pristine (non-infiltrated) and infiltrated activation layers. Figure 2a shows a cross-sectional SEM image of the interface between the dense membrane and the NFO-CTO activation layer. The activation layer is highly porous and shows a good attachment to the membrane surface. An enlarged view of the activation layer is given in Figure 2b. Grain sizes of NFO and CTO phases range between 50-100 nm, and both phases appear to be well intermixed. In Figure 2c, an activation layer is shown after infiltration and subsequent calcination at 850 ºC. Nanoparticles are deposited all over the surface of the porous NFO-CTO scaffold as needle-like structures of about 500 nm length. No significant pore blocking is observed when activating with Pr_6O_{11} (Figure S2), therefore catalyst infiltration is not expected to imply a hindrance in the gas flow through the porous layer.

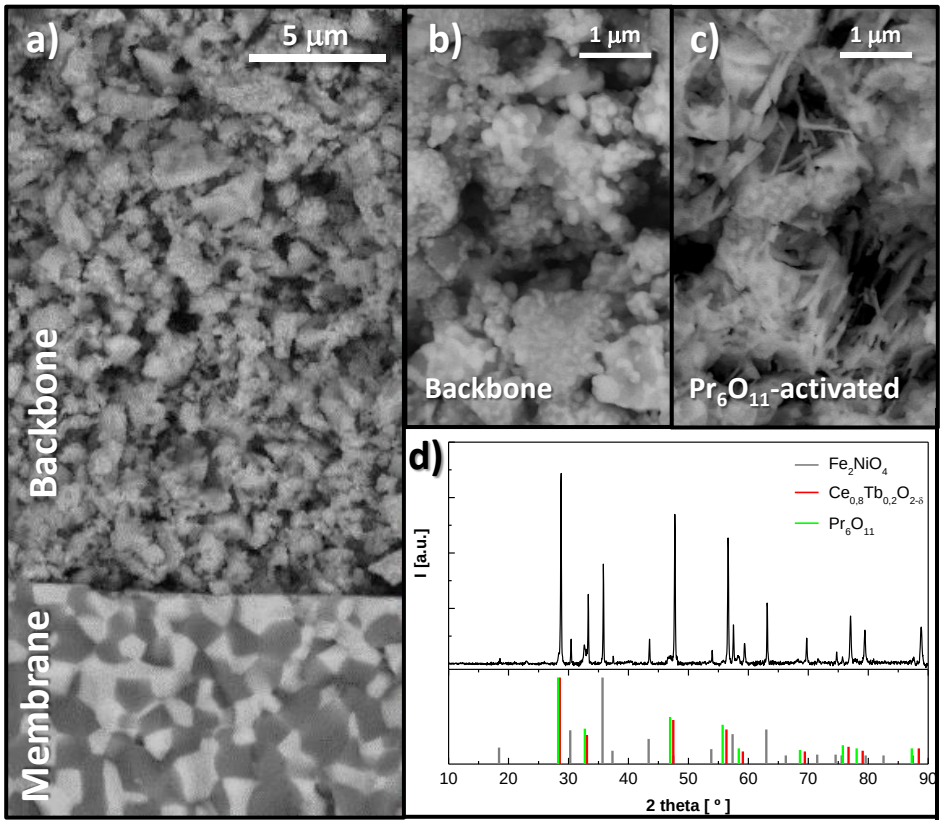

Figure 2: BSD-SEM images of activated NFO-CTO membranes: a) cross-sectional view of the porous scaffold/dense membrane interface of a non-infiltrated sample; bright grains represent the CTO phase and dark grains the NFO phase, magnification views of b) non-infiltrated composite scaffold, c) composite scaffold infiltrated with Pr_6O_{11} nanoparticles , d) XRD pattern of the Pr_6O_{11}-infiltrated activation layer.

XRD analysis revealed that the infiltrated catalyst after sintering in air at 850 ºC is present as Pr_6O_{11} particles[35]. Figure 2d shows the XRD pattern of the Pr_6O_{11}-activated layer, confirming the presence of NFO, CTO and Pr_6O_{11}. No evidence of impurity phases is found.

3.2. Oxygen permeation

Oxygen permeation measurements were performed on NFO-CTO membranes with thicknesses in the range of 0.6-0.7 mm. Three types of membranes were measured: (i) a bare membrane, (ii) a membrane on both sides coated with 30 µm-thick porous NFO-CTO layers, and (iii) a membrane having Pr_6O_{11} nanoparticles activating the porous NFO-CTO layers. In Figure 3a, the oxygen permeation fluxes for the three membranes measured under air/Ar gradient are plotted as a function of temperature. The addition of a porous NFO-CTO layer improves the oxygen flux from a value of 0.025 to 0.064 ml min^{-1} cm^{-2}, at 850 ºC, corresponding to a 2.5-fold improvement, while at 750 °C a 4-fold improvement is observed. The enhancement in oxygen flux induced by the deposition of porous layers on both membrane surfaces can be ascribed to the concomitant increase in specific surface area (Figure 1) and, thus, in the number of TPB sites available for oxygen exchange. Similar improvements in the oxygen flux obtained via surface activation of single-phase membranes through deposition of porous layers have been reported previously [36, 37]. For the dual-phase NFO-CTO membrane, the porous fine-grained NFO-CTO layers provide much

larger numbers of TPB sites compared to the bare membrane surface, facilitating the oxygen reduction and evolution kinetics (see also Fig. 1) [38, 39]. The improvement in the oxygen permeation flux becomes more significant for the membrane presenting Pr_6O_{11} nanoparticles in the porous NFO-CTO layers. A 6-fold improvement is obtained at 850 ºC reaching an oxygen flux of 0.14 ml min^{-1} cm^{-2}. At lower temperatures the positive effect of membrane activation is even more evident: a 12-fold increase is found at 750 ºC with respect to the bare membrane, thus confirming the promoting effect on the surface exchange reactions, typically limiting permeation at these temperatures.

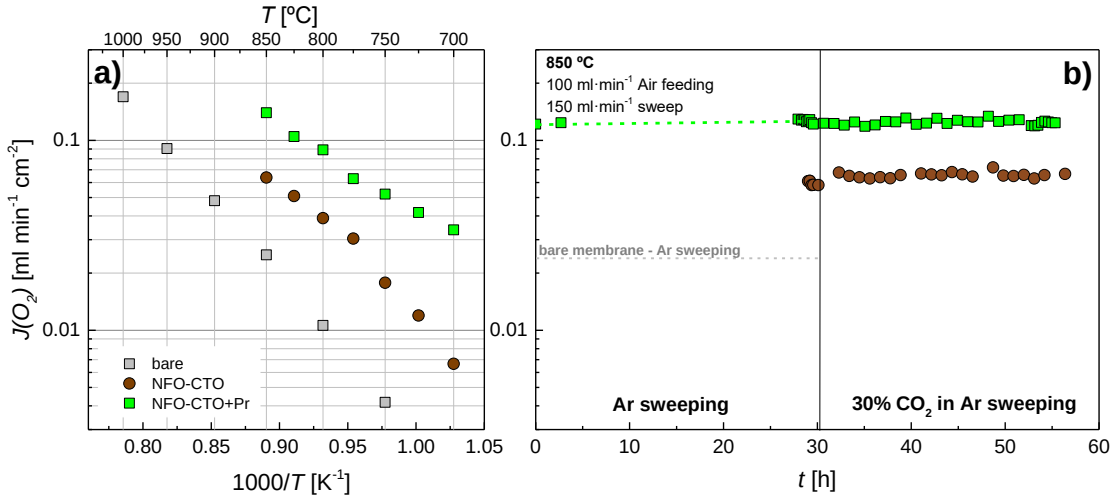

Figure 3: a) Temperature dependence of the oxygen flux for (i) bare NFO-CTO membrane (labeled bare), (ii) a membrane with NFO-CTO activation layers (labeled NFO-CTO), and (iii) a membrane after activation of the NFO-CTO activation layers with Pr_6O_{11} nanoparticles (labeled NFO-CTO+Pr), and b) oxygen permeation of the membranes with non-infiltrated and infiltrated activation layers, at 850 °C, as a function of time for different sweep gases. The grey dashed line depicts the oxygen flux for the bare membrane at 850 °C measured under an air/Ar gradient as shown in figure (a).

Additionally, oxygen permeation was studied over a prolonged time to investigate the stability of the activated membrane at work (Figure 3b). First, the NFO-CTO+Pr coated membrane was subjected to an air/argon gradient at 850 °C for 30 hours. After this, no significant change in the permeation rate was found. The value of $J(O_2)$ stabilized at 0.13 ml min^{-1} cm^{-2}. Subsequently, the sweep gas was changed to a 30% CO_2 in Ar mixture (mimicking oxyfuel conditions with respect to pCO_2) while the feed gas was not changed. Initially, $J(O_2)$ dropped slightly to 0.12 ml min^{-1} cm^{-2}. During the following 24 hours on stream, the Pr_6O_{11}-activated membrane exhibited stable behavior. Regarding the NFO-CTO coated membrane (labeled as NFO-CTO), similar test conditions were applied with a continuous 30% CO_2 in Ar sweeping during 24 h. In contrast to the Pr_6O_{11}-activated layer, the oxygen flux increases to a value of 0.067 ml min^{-1} cm^{-2} upon switching to CO_2 as sweep gas. This beneficial effect of CO_2 as sweep gas has been previously observed for the case of NFO-CTO membranes above 850 ºC[20, 22]. This is ascribed to the better sweeping properties and higher thermal emissivity of CO_2 with respect to Ar, thus producing a local increase of temperature on membrane surface and subsequently improving oxygen permeation. The small loss in oxygen flux of the membrane with Pr_6O_{11}-activated NFO-CTO layers can be related with a stronger CO_2 adsorption on the active sites generated by Pr_6O_{11} activation, hindering this way the oxygen reduction reactions involved in the oxygen permeation.

3.3. Pulse isotopic exchange

PIE measurements clearly demonstrate that the Pr_6O_{11}-activated NFO-CTO composite powder is much more active than the bare (i.e., non-activated) NFO-CTO powder for oxygen exchange. Figure 4 shows the oxygen isotope fractions as a function of temperature for both materials. At a temperature of around 800 °C, about half of the original fraction of $^{18}O_2$ in the pulse volume is converted into $^{16}O_2$ and $^{16}O^{18}O$ for the bare composite powder, whereas this temperature is lowered to about 570 °C after activation with Pr_6O_{11}.

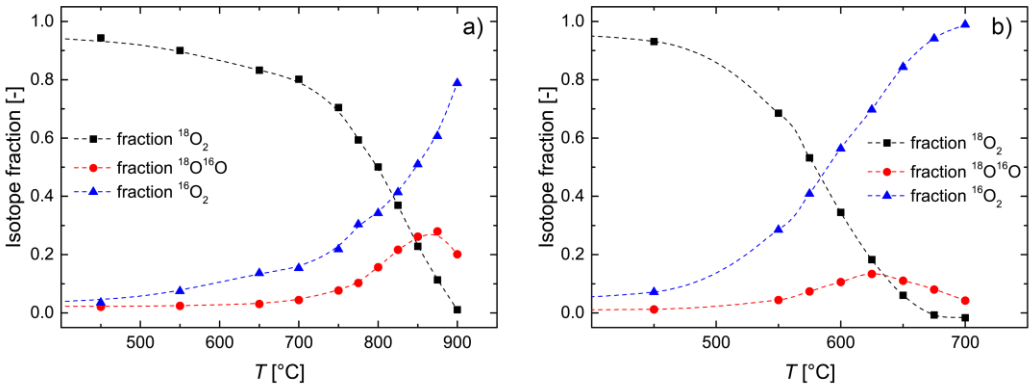

Figure 4: Oxygen isotope fractions as a function of temperature from PIE measurements, at pO_2 = 0.21 atm, on powders of a) NFO-CTO and b) NFO-CTO activated with Pr_6O_{11}. Dashed lines serve as guides to the eye.

Figure 5 shows the calculated surface exchange rates ($\Re_0$) of the bare and Pr_6O_{11}-activated NFO-CTO powders as well as corresponding values derived from measurements on powders of the individual NFO and CTO phases. The results show that NFO exhibits poor oxygen exchange kinetics, this is attributed to a low oxygen vacancy concentration of this material [40]. The values of $\Re_0$ for bare NFO-CTO and CTO are close to each other above ~725 °C, suggesting that it is mainly the CTO phase that determines the exchange rate found for the composite. The observation that the bare composite exhibits a higher value of $\Re_0$ below ~725 °C than both constituents is interpreted to reflect a synergy between both phases. The enhanced exchange rate at these low temperatures might be due to the availability of electrons provided by the NFO phase. This effect is further observed for composites with different NFO to CTO ratios (cf. Figure S3). However, more research is needed to explain this observation. Furthermore, the exchange rate of NFO-CTO is increased by more than one order of magnitude after activation with Pr_6O_{11} nanoparticles (Figure 5), in line with permeation results (Figure 3) and previous reports on SOFC cathodes [27-29, 44]. With regard to the activation energies, it is observed a significant difference for the Pr_6O_{11}-activated NFO-CTO sample with a diminution in the values

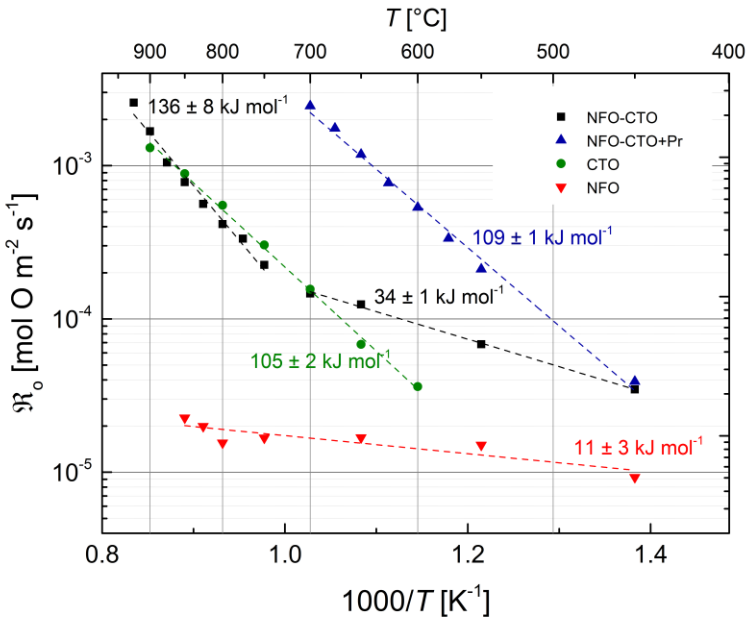

Figure 5. Temperature dependence of the surface exchange rate of NFO, CTO, non-activated and Pr_6O_{11}-activated NFO-CTO composite powders. Activation energies are specified for each of the materials; for NFO-CTO two different energies are calculated for the regions above and below 700 °C.

3.4. Electrochemical characterization

To further investigate the catalytic effect of Pr_6O_{11} addition into the NFO-CTO activation layers, EIS measurements were performed on NFO-CTO/CGO/NFO-CTO symmetrical cells. Figures 6a and 6b show impedance spectra of cells with non-activated and Pr_6O_{11}-activated NFO-CTO electrodes recorded in air, 5% of O_2 in N_2, and 5% of O_2 in CO_2 after subtraction of the apparent electrolyte resistance. The polarization resistance (R_p) increases for both electrodes when switching from air to gases with 5% of O_2 as well as after the replacement of N_2 by CO_2. That phenomenon should be ascribed to the reduction of the available oxygen on the electrode surface for the oxygen reduction reaction. In the case where the atmosphere is changed from air to 5% of O_2, the increase of the R_p is only related with the lower oxygen partial pressure in the electrode, worsening the surface processes and increasing the resistance of the low frequency processes. On the other hand, CO_2 competes with O_2 for the oxygen reduction reaction active sites, reducing the active electrode surface. That issue mainly affects the resistance at low frequencies (surface processes) and shift the relaxation frequency to lower values. After Pr_6O_{11} activation of the NFO-CTO electrodes, R_p is decreased by one order of magnitude regardless of the atmosphere composition. Figure 6c and 6d show the corresponding Bode plots for both electrodes under the three atmospheres and reveals that Pr_6O_{11} activation ameliorates processes appearing at frequencies ranging from 0.1 to 10 Hz.

EIS spectra fitting using the proposed equivalent circuit provides further evidence about the magnitude and origin of this improvement (cf. Figure 6e-g and S4). In the case of the pristine NFO-CTO electrode, two arcs could be distinguished: one at low frequencies (LF1, 1-4 Hz), and another at high frequencies (HF, 15-16 kHz). The low frequency arcs are usually related to surface

processes such as oxygen adsorption, dissociation, or reduction [41-43]. The LF arc is reduced upon Pr_6O_{11} activation. However, in Pr_6O_{11}-activated electrode, two arcs are present in the Nyquist spectrum, one at low frequencies (LF2, 1-2 Hz) and another one at medium frequencies (MF, 200-500 Hz).Both arcs are one or even two order of magnitude smaller that the LF1 resistance of the pristine sample. This effect is attributed to the above-observed enhancement of the surface exchange reaction. In addition, the contribution of HF processes decreases, and this can be assigned to transport properties of Pr_6O_{11} oxide covering the NFO-CTO electrode surface, which may favor the surface transport of both oxygen species and electron holes [27, 28]. Furthermore, Pr_6O_{11} possesses relatively high electronic conductivity and improve the oxygen surface processes [27, 28, 44] and the surface exchange rate at the tested temperatures (Figure 5).

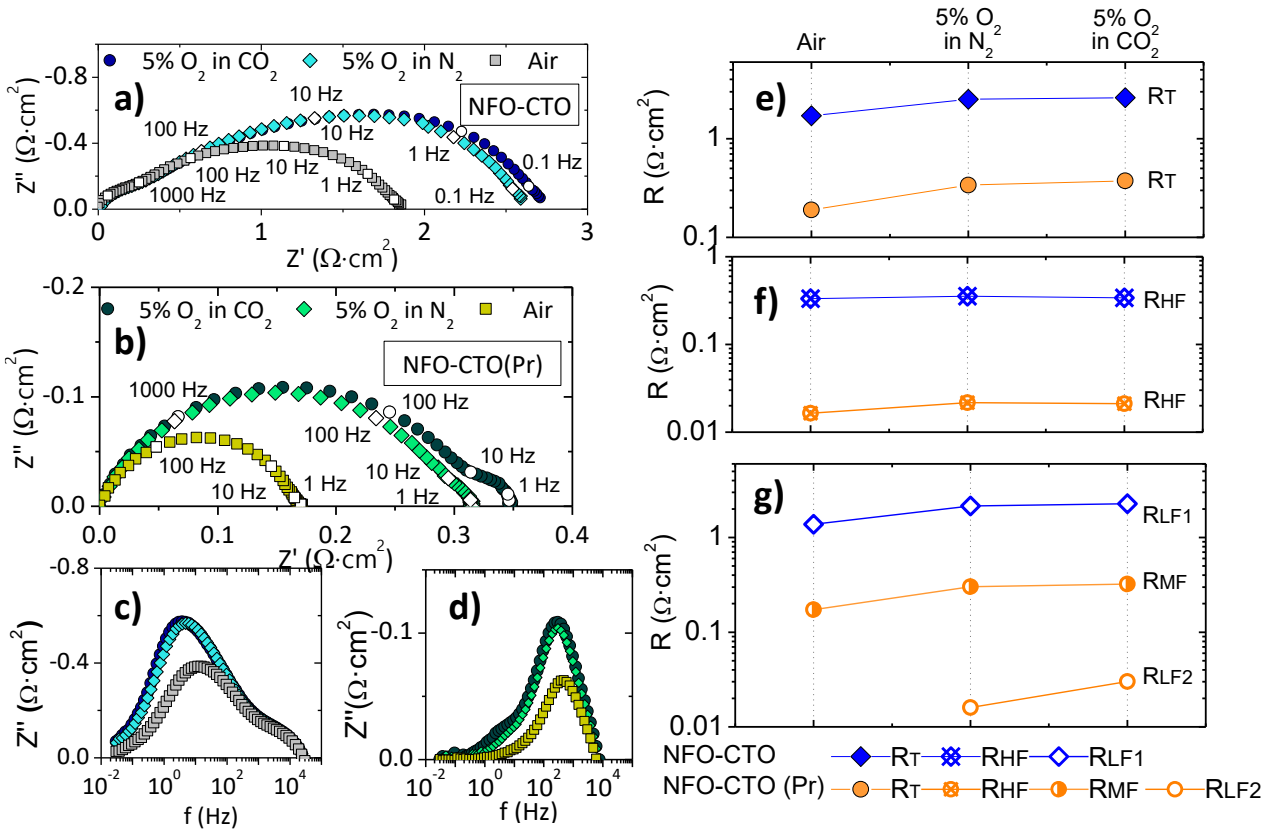

Figure 6. (a) Nyquist plot of NFO-CTO, (b) Nyquist plot of NFO-CTO (Pr), (c-d) Bode plots, (e) polarization resistance, (f) fitting results of the bare and Pr_6O_{11}-impregnated NFO-CTO electrode in different atmospheres at 850 °C at high frequency and (g) low and medium frequencies.

The influence of different atmospheres on the electrochemical performance was further studied. The dependency of the resistance on the oxygen partial pressure ($R \propto pO_2^{-mi}$) can shed further light on the nature of the limiting steps in the oxygen reduction process [45-47]. The fitting results are shown in Figure 6 and supplementary information (Figure S5). The untreated electrode shows a pO_2-independent contribution at HF, which can be assigned to solid-state oxide-ion transport through the composite. Nevertheless, the infiltrated NFO-CTO electrode presents a small dependence ($m_{HF} \approx 0.19$ in $R_{HF} \propto pO_2^{-mi}$) with oxygen partial pressure that can be ascribed to the p-type electronic conductivity ($\sigma \approx pO_2^{1/6}$) conferred by the Pr_6O_{11} infiltrated. As Figure 6f shows, the LF1 resistance of the non-infiltrated electrode is pO_2-dependent ($m_{LF1} \approx 0.32$ in $R_{LF} \propto pO_2^{-mi}$) and can be related with the diffusion of atomic oxygen species and charge transfer ($O_{ads} + e^- \rightarrow$

O_{ads}^{-}) [42, 48]. In the case of treated electrode, the resistance at medium frequency (MF, $m_{MF} \approx 0.38$) can be assigned to the same limiting process, but in this case the resistance is reduced by more than one order of magnitude. The activation of the layer with Pr_6O_{11} enhances the reduction of the adsorbed oxygen and shifts the frequency to higher values[49].

The coupled effect of low pO_2 and presence of CO_2 was studied with the Pr_6O_{11}-activated NFO-CTO electrodes and aims to mimic membrane sweeping conditions. CO_2 induces the rise in MF and LFs resistances and this stems from the competitive adsorption of O_2 and CO_2 at the active sites, having a stronger effect for the Pr_6O_{11}-activated sample with a higher increase in LF2 resistance (Figure 6c). This increase in MF and LF frequencies when the electrodes were contacted with CO_2 is in agreement with results from oxygen permeation experiments (Figure 3b) in which $J(O_2)$ of the Pr_6O_{11}-activated membrane slightly decreased when switching to a CO_2-containing atmosphere. Furthermore, the bulk transport properties of the electrode are not influenced by the CO_2 presence, since the resistance at HF remains constant [50].

4. Conclusions

NFO-CTO dual-phase composite membranes were coated on both sides with 30 μm-thick porous scaffolds of the fine-grained NFO-CTO that were further activated with Pr_6O_{11} nanoparticles to enhance surface exchange kinetics. Measurements in the temperature range 850 – 700 ºC revealed a 2-4 fold increase of the oxygen flux after coating porous NFO-CTO layers on both sides of the dense membrane, and a 6-12 fold increase relative to the bare membrane after activation with Pr_6O_{11} nanoparticles into both coated layers. No degradation of the oxygen fluxes was found in CO_2-containing atmospheres, illustrating the potential use of the developed NFO-CTO membranes in oxyfuel applications.

PIE measurements confirmed an increased exchange rate of composite NFO-CTO powders by more than one order of magnitude after activation with Pr_6O_{11} nanoparticles. Furthermore, EIS measurements on NFO-CTO/CGO/NFO-CTO symmetrical cells showed a strong decrease in the polarization resistance after Pr_6O_{11} activation of the porous NFO-CTO electrodes. The present results demonstrate that addition of Pr_6O_{11} nanoparticles into porous activation layers is a promising route to enhance oxygen permeation fluxes across dual-phase membranes.

5. Conflicts of interest

There are no conflicts of interest to declare.

6. Acknowledgments

Financial support by the EU through FP7 GREEN-CC Project (Grant Agreement Number: 608524). The Spanish Government (ENE2014-57651 and SEV-2016- 0683 grants) is gratefully acknowledged.

SUPPORTING INFORMATION

Figure S1. BSD-SEM fracture cross-section view of a NFO-CTO membrane after sintering at 1400 ºC for 10 h.

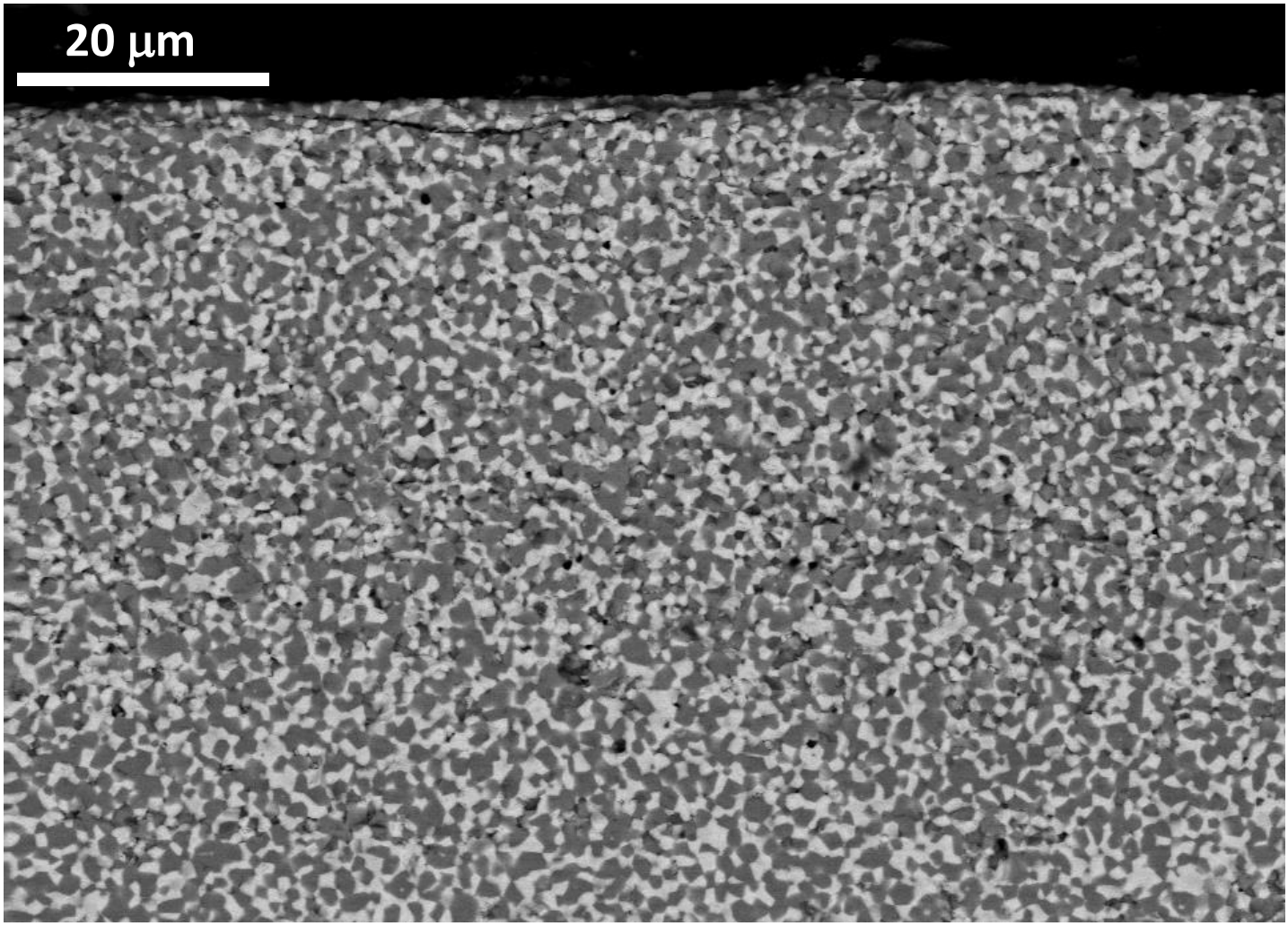

Figure S2.BSD-SEM pictures of a) NFO-CTO backbone and b) NFO-CTO backbone activated with Pr_6O_{11} nanoparticles.

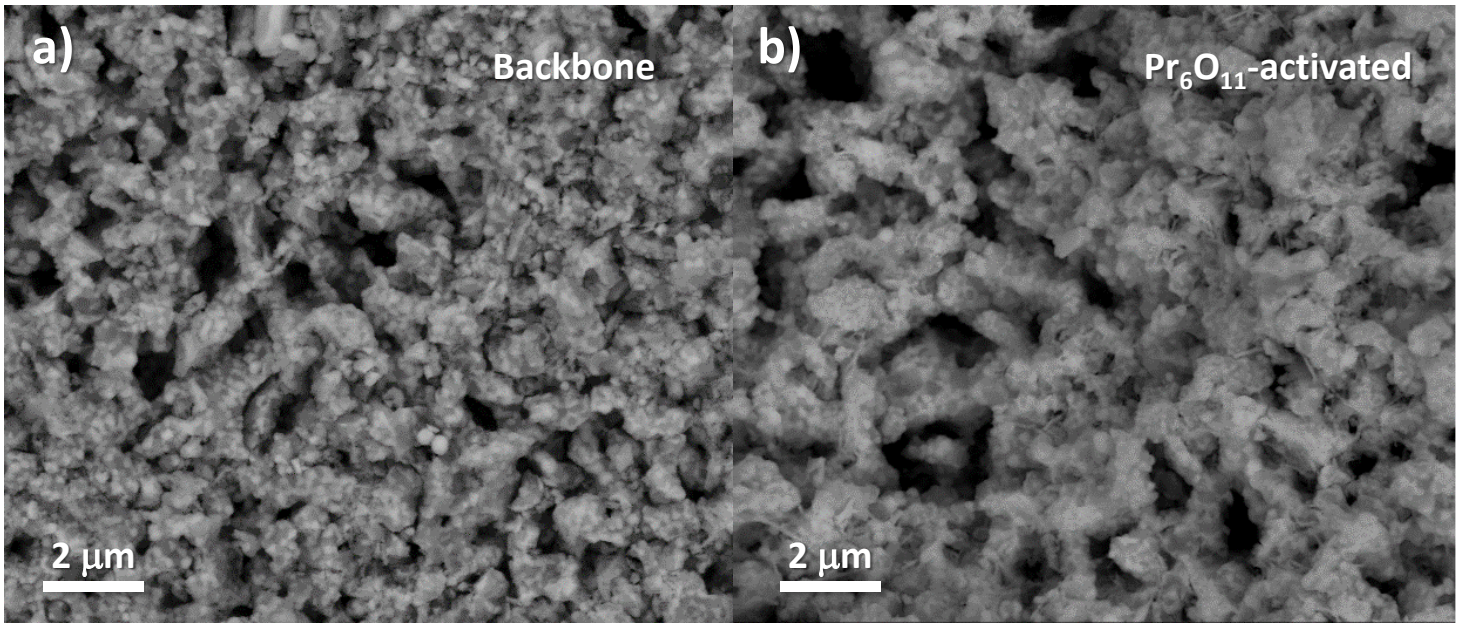

Figure S3. Overall exchange rate measured by PIE for composite powders with different vol. ratios of the components.

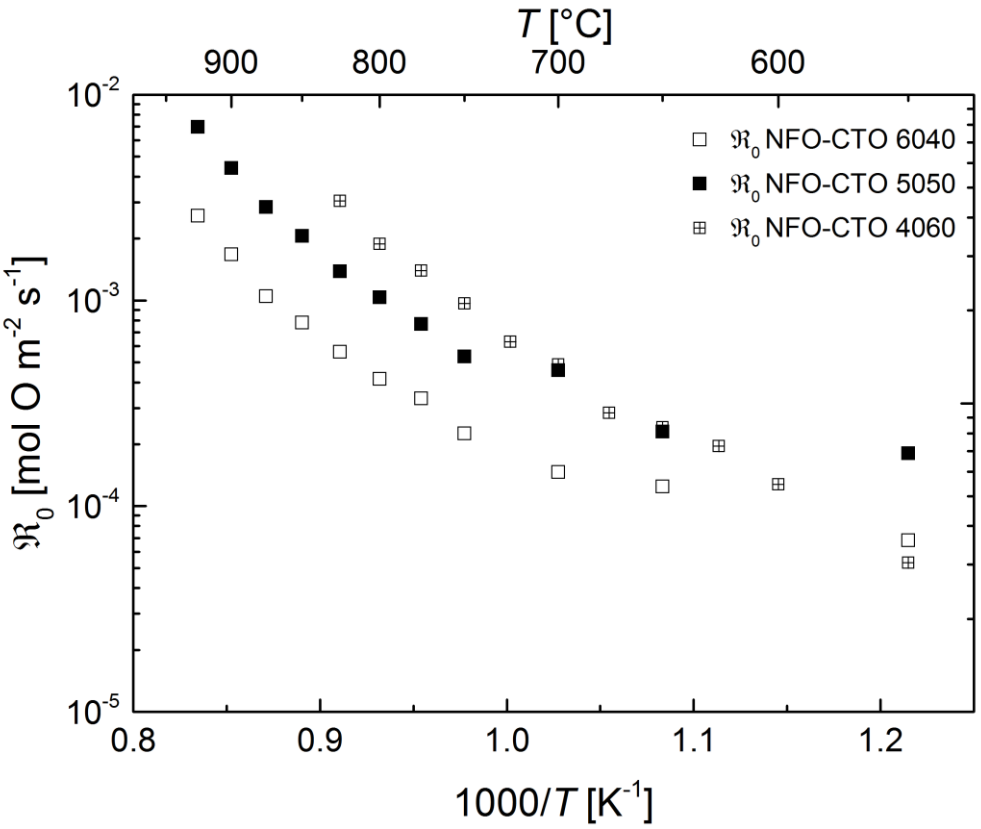

Figure S4. Capacitance (a) and frequency (b) obtained from the fitting of the electrochemical impedance spectrums in different atmospheres at 850 ºC.

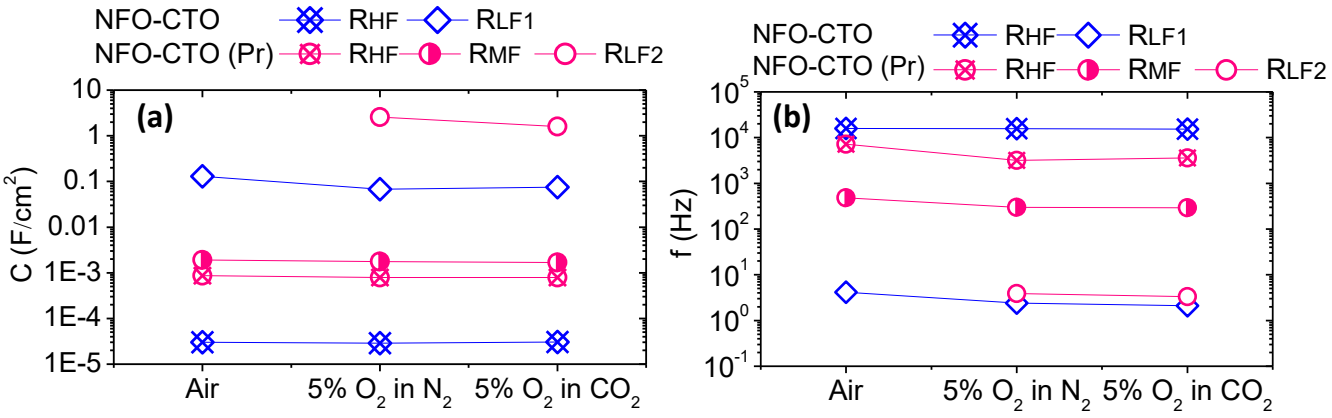

Figure S5. Oxygen partial pressure dependence of the Pr_6O_{11}-activated and non-treated NFO-CTO fitting results at 850 ºC.

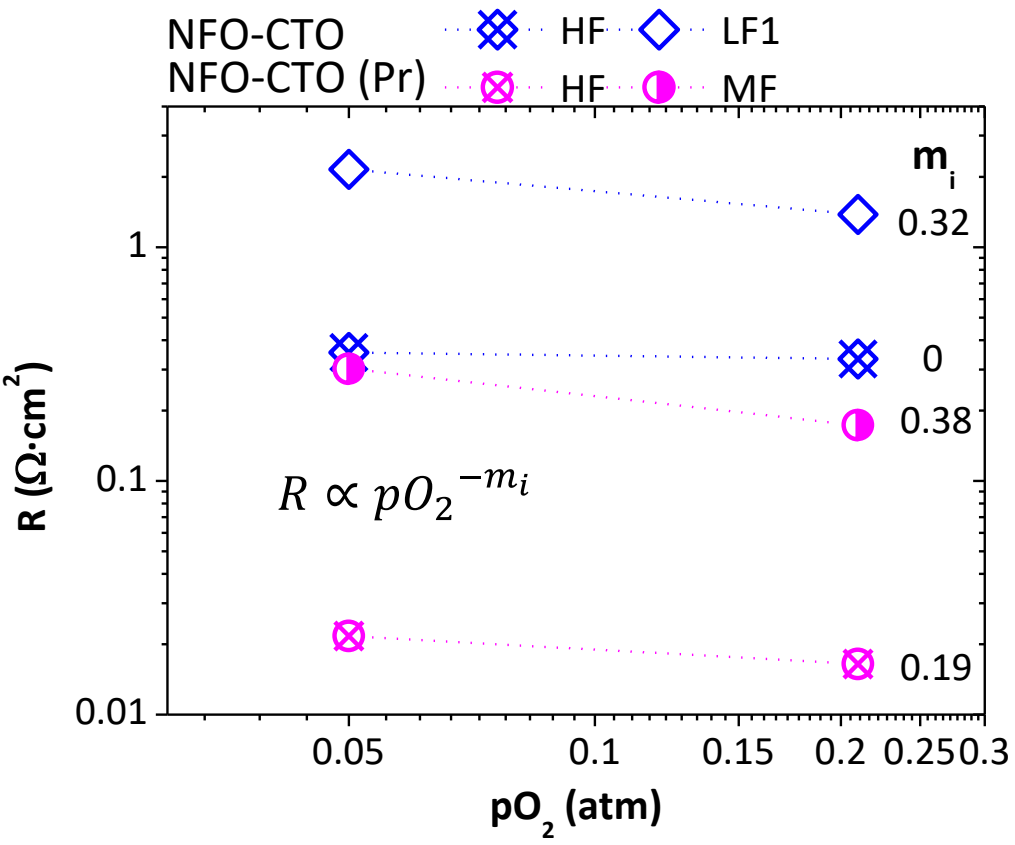

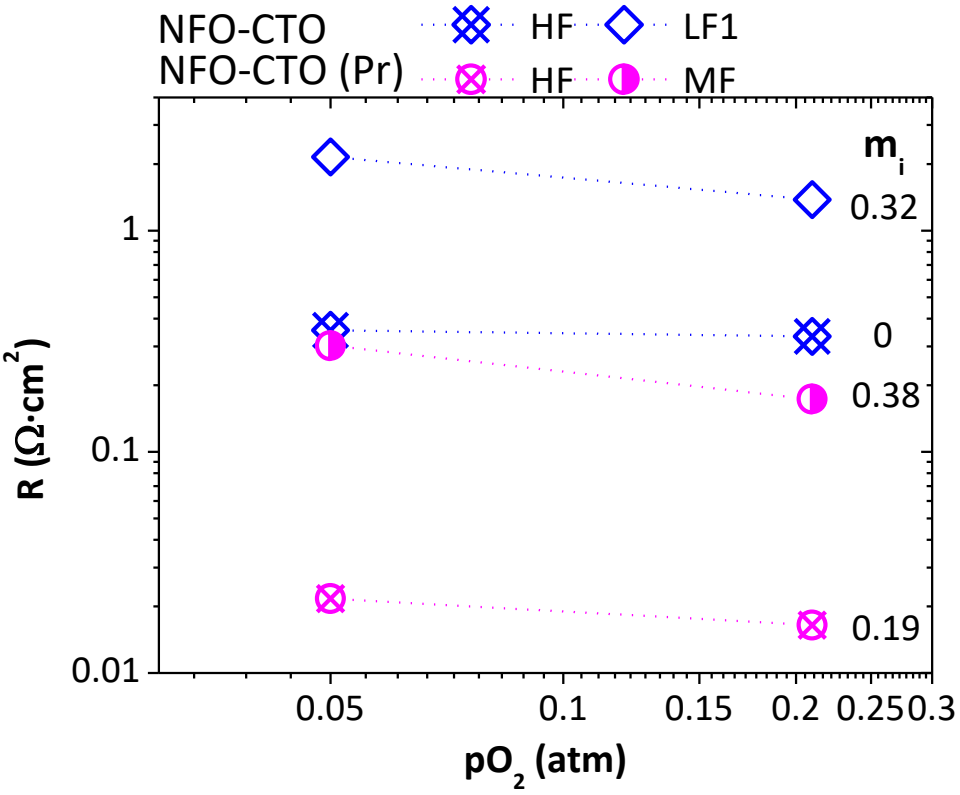
NFO-CTO
NFO-CTO (Pr)
HF
LF1
HF
MF
m_i
0.32
0
0.38
0.19
1
0.1
0.01
R (Ω·cm²)
0.05
0.1
0.15
0.2
0.25
0.3
pO2 (atm)

REFERENCES

1. J. Emsley, *Nature's Building Blocks: An A-Z guide to the elements*, 2001.
2. A. Bose, G. Stiegel, P. Armstrong, B. Halper and E. P. Foster, in *Inorganic Membranes for Energy and Environmental Applications*, ed. A. Bose, Springer New York, 2009, DOI: 10.1007/978-0-387-34526-0_1, ch. 1, pp. 3-25.
3. P. T. E. d. CO2, *Usos del CO2: un camino hacia la sostenibilidad*, 2013.
4. M. den Exter, W. Haije and J. Vente, in *Inorganic Membranes for Energy and Environmental Applications*, ed. A. Bose, Springer New York, 2009, DOI: 10.1007/978-0-387-34526-0_2, ch. 2, pp. 27-51.
5. M. A. Habib, H. M. Badr, S. F. Ahmed, R. Ben-Mansour, K. Mezghani, S. Imashuku, G. J. la O, Y. Shao-Horn, N. D. Mancini, A. Mitsos, P. Kirchen and A. F. Ghoneim, *International Journal of Energy Research*, 2011, **35**, 741-764.
6. S. S. Hashim, A. R. Mohamed and S. Bhatia, *Renewable & Sustainable Energy Reviews*, 2011, **15**, 1284-1293.
7. P. Markewitz, J. Marx, A. Schreiber and P. Zapp, *Ghgt-11*, 2013, **37**, 2864-2876.
8. T. Takahashi, T. Esaka and H. Iwahara, *Journal of Solid State Chemistry*, 1976, **16**, 317-323.
9. B. Cales and J. F. Baumard, *Journal of Materials Science*, 1982, **17**, 3243-3248.
10. B. Cales and J. F. Baumard, *Journal of the Electrochemical Society*, 1984, **131**, 2407-2413.
11. S. Baumann, J. M. Serra, M. P. Lobera, S. Escolastico, F. Schulze-Kueppers and W. A. Meulenberg, *Journal of Membrane Science*, 2011, **377**, 198-205.
12. C. Gaudillere, J. Garcia-Fayos and J. Serra, *Journal of Materials Chemistry A*, 2013, DOI: 10.1039/c3ta14069e.
13. C. Niedrig, S. Taufall, M. Burriel, W. Menesklou, S. F. Wagner, S. Baumann and E. Ivers-Tiffée, *Solid State Ionics*, 2011, **197**, 25-31.
14. M. Arnold, H. Wang and A. Feldhoff, *Journal of Membrane Science*, 2007, **293**, 44-52.
15. J. Yi, M. Schroeder, T. Weirich and J. Mayer, *Chemistry of Materials*, 2010, **22**, 6246-6253.
16. J. Yi and M. Schroeder, *Journal of Membrane Science*, 2011, **378**, 163-170.
17. H. Luo, T. Klande, Z. Cao, F. Liang, H. Wang and J. Caro, *Journal of Materials Chemistry A*, 2014, **2**, 7780-7787.
18. K. S. Yun, C.-Y. Yoo, S.-G. Yoon, J. H. Yu and J. H. Joo, *Journal of Membrane Science*, 2015, **486**, 222-228.
19. J. H. Joo, K. S. Yun, J.-H. Kim, Y. Lee, C.-Y. Yoo and J. H. Yu, *Acs Applied Materials & Interfaces*, 2015, **7**, 14699-14707.
20. M. Balaguer, J. Garcia-Fayos, C. Solis and J. M. Serra, *Chemistry of Materials*, 2013, **25**, 4986-4993.
21. C. Gaudillere, J. Garcia-Fayos, M. Balaguer and J. M. Serra, *Chemsuschem*, 2014, **7**, 2554-2561.
22. J. Garcia-Fayos, M. Balaguer and J. M. Serra, *ChemSusChem*, 2015, DOI: 10.1002/cssc.201500951, n/a-n/a.
23. H. J. M. Bouwmeester, *Catalysis Today*, 2003, **82**, 141-150.
24. H. Pan, L. Li, X. Deng, B. Meng, X. Tan and K. Li, *Journal of Membrane Science*, 2013, **428**, 198-204.
25. M. P. Lobera, M. Balaguer, J. Garcia-Fayos and J. M. Serra, *Chemcatchem*, 2012, **4**, 2102-2111.

26. D. Ding, X. X. Li, S. Y. Lai, K. Gerdes and M. L. Liu, *Energy & Environmental Science*, 2014, **7**, 552-575.
27. L. Navarrete, C. Solis and J. M. Serra, *Journal of Materials Chemistry A*, 2015, **3**, 16440-16444.
28. C. Nicollet, A. Flura, V. Vibhu, A. Rougier, J.-M. Bassat and J.-C. Grenier, *International Journal of Hydrogen Energy*, DOI: http://dx.doi.org/10.1016/j.ijhydene.2016.04.024.
29. R. Chiba, H. Aono and K. Kato, in *Solid Oxide Fuel Cells 13*, eds. T. Kawada and S. C. Singhal, 2013, vol. 57, pp. 1831-1840.
30. M. Balaguer, C. Solís and J. M. Serra, *The Journal of Physical Chemistry C*, 2012, **116**, 7975-7982.
31. C. Solís, M. Balaguer, F. Bozza, N. Bonanos and J. M. Serra, *Applied Catalysis B: Environmental*, 2014, **147**, 203-207.
32. H. J. M. Bouwmeester, C. Song, J. Zhu, J. Yi, M. van Sint Annaland and B. A. Boukamp, *Physical Chemistry Chemical Physics*, 2009, **11**, 9640-9643.
33. H. J. M. Bouwmeester, C. Song, J. Zhu, J. Yi, M. v. S. Annaland and B. A. Boukamp, *Physical Chemistry Chemical Physics*, 2009, **11**, 9640-9643.
34. C.-Y. Yoo, B. A. Boukamp and H. J. M. Bouwmeester, *Journal of Solid State Electrochemistry*, 2011, **15**, 231-236.
35. H. E. Swanson and S. United, *Standard x-ray diffraction powder patterns*, U.S. Dept. of Commerce, National Bureau of Standards : For sale by the Supt. of Docs., U.S. G.P.O., Washington, DC, 1953.
36. J. M. Serra, J. Garcia-Fayos, S. Baumann, F. Schulze-Kueppers and W. A. Meulenberg, *Journal of Membrane Science*, 2013, **447**, 297-305.
37. C. Gaudillere, J. Garcia-Fayos and J. M. Serra, *ChemPlusChem*, 2014, DOI: 10.1002/cplu.201402142, n/a-n/a.
38. J. H. Joo, K. S. Yun, Y. Lee, J. Jung, C. Y. Yoo and J. H. Yu, *Chemistry of Materials*, 2014, **26**, 4387-4394.
39. M. Ramasamy, S. Baumann, J. Palisaitis, F. Schulze-Kuppers, M. Balaguer, D. Kim, W. A. Meulenberg, J. Mayer, R. Bhave, O. Guillon and M. Bram, *Journal of the American Ceramic Society*, 2016, **99**, 349-355.
40. X. Shi, Y.-F. Li, S. L. Bernasek and A. Selloni, *Surface Science*, 2015, **640**, 73-79.
41. S. B. Adler, *Chem. Rev.*, 2004, **104**, 4791-4843.
42. J. D. Kim, G. D. Kim, J. W. Moon, Y. I. Park, W. H. Lee, K. Kobayashi, M. Nagai and C. E. Kim, *Solid State Ionics*, 2001, **143**, 379-389.
43. M. J. Jorgensen and M. Mogensen, *Journal of the Electrochemical Society*, 2001, **148**, A433-A442.
44. V. Thangadurai, R. A. Huggins and W. Weppner, *Journal of Solid State Electrochemistry*, 2001, **5**, 531-537.
45. R. R. Peng, T. Z. Wu, W. Liu, X. Q. Liu and G. Y. Meng, *J. Mater. Chem.*, 2010, **20**, 6218-6225.
46. F. H. vanHeuveln and H. J. M. Bouwmeester, *Journal of the Electrochemical Society*, 1997, **144**, 134-140.
47. Y. Takeda, R. Kanno, M. Noda, Y. Tomida and O. Yamamoto, *Journal of The Electrochemical Society*, 1987, **134**, 2656-2661.
48. R. Peng, T. Wu, W. Liu, X. Liu and G. Meng, *J. Mater. Chem.*, 2010, **20**, 6218-6225.
49. F. Mauvy, C. Lalanne, J. M. Bassat, J. C. Grenier, H. Zhao, L. H. Huo and P. Stevens, *Journal of the Electrochemical Society*, 2006, **153**, A1547-A1553.
50. V. B. Vert and J. M. Serra, *J. Power Sources*, 2011, **196**, 4270-4276.